THE ASTROPHYSICAL JOURNAL, 547:475–490, 2001 January 20

SIMULATIONS OF THE PHOTOSPHERIC MAGNETIC ACTIVITY AND OUTER ATMOSPHERIC RADIATIVE LOSSES OF COOL STARS BASED ON CHARACTERISTICS OF THE SOLAR MAGNETIC FIELD

CAROLUS J. SCHRIJVER
Stanford-Lockheed Institute for Space Research, Department L9-41, Building 252, 3251 Hanover Street, Palo Alto, CA 94304; schryver@lmsal.com
Received 2000 March 7; accepted 2000 September 12

ABSTRACT

The observed disk-integrated radiative losses from the outer atmospheres of stars with convective envelopes are determined by the distribution of magnetic field over their surfaces. Earlier modeling of the random walk transport of the solar photospheric magnetic field with the classical Leighton model has given us insight into how field patterns form and evolve on large scales. This paper presents the first comprehensive simulations of the dynamic photospheric magnetic field of the Sun down to the scale of the mixed polarity network, thus incorporating all flux involved in outer atmospheric heating. The algorithm incorporates the classical diffusion model but includes ephemeral regions (which populate the network that contributes significantly to the disk-integrated chromospheric emission) and the early phase of decay of active regions (which is important for the field patterns in very active stars). Moreover, individual flux concentrations are tracked and subjected to collisions and fragmentation, and the flux dispersal is made dependent on the flux contained in the concentrations, as observed on the Sun. The latter modification causes the model to be nonlinear. Tests demonstrate that the new model successfully describes the solar magnetic field.

The model is then used to simulate the field on other cool stars covering several orders of magnitude in activity and to estimate the surface-averaged radiative losses associated with that field. The stellar extrapolations are based on the statistical properties of solar bipolar regions throughout the cycle. Simulations in which only the frequency of flux emergence is changed to simulate stars of different activity are shown to be consistent with the observed nonlinear relationships between disk-averaged radiative losses from chromospheres and coronae of cool stars. Consequently, the properties of the solar magnetic field from small ephemeral regions up to large active regions are compatible with stellar observations. Stellar observations suggest that those field properties are not the only ones that can explain the flux-flux relationships, however, because also stars with polar spots or persistent active longitudes obey these same flux-flux relationships.

The model is also used to understand how rapidly flux is processed in stellar photospheres in stars with activity patterns like the Sun: the average total absolute magnetic flux $\langle \Phi_* \rangle$ (Mx) at the stellar surface is found to be proportional to the mean rate of flux emergence and cancellation $\langle E_* \rangle$ (Mx s^{-1}) within the range from $\frac{1}{10}\langle E_\odot \rangle$ up to $10\langle E_\odot \rangle$, where $\langle E_\odot \rangle$ is the flux injection rate for the active Sun. This linearity is primarily a consequence of an activity-dependent change in the shape of the flux histogram for emerging bipoles. This change reflects that active regions and ephemeral regions have a different dependence on dynamo strength. The implications of the results of the simulations for the dynamo and for the relationship between activity and stellar rotation are discussed.

Subject headings: stars: activity — stars: magnetic fields — Sun: activity — Sun: magnetic fields

1. INTRODUCTION

The outer atmospheric activity of cool stars like the Sun is driven by the evolving magnetic fields in their photospheres. The photospheric field extends into the stellar outer atmosphere, where the field causes nonradiative energy to be deposited. This energy is distributed over the chromosphere, the corona, and the interface between them that is referred to as the transition region. Outer atmospheric radiative losses from the Sun and stars hold important clues on the distribution of magnetic flux over their surfaces. The central focus of this study is to establish what we can infer from observations of stellar atmospheric activity about the stellar photospheric magnetic field and, ultimately, how we can use that information to probe stellar dynamos. The present study primarily examines two questions: (1) are the properties of the Sun's magnetic field compatible with the observations of other cool stars? and (2) how much does the comparison of the Sun and stars constrain the properties of the flux source function and of flux dispersal on other stars?

The solar magnetic field and the outer atmospheric responses to it are so complicated that there is no hope of deducing the field geometry of distant stars from disk-integrated observations. Moreover, ab initio simulations of surface magnetic activity in stars are at present impossible because existing dynamo models cannot predict the properties of emerging bipolar regions. Instead, an approach to exploit the information that stellar observations contain about the surface magnetic field and about the dynamo is to compare the observations to numerical simulations.

The large-scale solar photospheric field has been modeled successfully by the traditional surface diffusion model for the evolution of magnetic flux over the solar surface as developed by Leighton, Sheeley, Wang, and colleagues.

However, a meaningful comparison of the Sun and stars requires that the flux dispersal model applies not only to the large-scale field for which it was originally developed. In addition to that, it should also describe the mixed polarity network because that dominates the chromospheric emission from the Sun as a star and is increasingly more important as activity decreases. It also should incorporate a flux-dependent field dispersal because that governs the initial decay of active regions and therefore is important in the modeling of active stars.

To include these extremes of solar activity in the model, I formulate numerical recipes for flux transport that are based on solar observations. With these, the diffusion model can be used on all scales, for the first time allowing a complete description of all of the solar field involved in outer atmospheric heating. The emergence frequency of ephemeral regions is so high that modeling based on observed emergences is impractical. Moreover, the simulations of stars require some statistical approach. Hence, the flux injection is described by a combination of random processes, capturing the ensemble properties of emerging flux on the Sun throughout the cycle.

These and other numerical recipes are used to simulate the surface activity of stars of very different activity levels. The magnetic field simulations are subsequently used to compute the expected radiative losses from chromospheres, coronae, and transition regions. These are then compared to the observed relationships between these measures of stellar activity to study to what extent the Sun is characteristic of other cool stars.

The properties of the emergence, dispersal, and disappearance of the solar photospheric magnetic field are summarized in § 2 but discussed in more detail in Appendix A. The dependence of the simulations on the numerical recipes and constants is evaluated in § 3 where the results are compared to solar observations. Simulations of stars of different levels of activity are discussed in § 4. The mean rate at which flux is processed in the photosphere is calibrated against the mean photospheric flux in § 5. Stellar flux-flux relationships are discussed in § 6. The final section summarizes the conclusions and discusses them in the context of cool star studies in general.

2. THE SOLAR MAGNETIC FIELD AND THE NUMERICAL ALGORITHM

Simulations of the magnetic field of the Sun and other cool stars require knowledge about three processes: (1) the emergence of flux from the interior, (2) the dispersal of flux over the surface, and (3) the disappearance of flux from the photosphere. This section outlines what is known about these components and is needed for the model. The quantitative details and numerical recipes are described in Appendix A.

2.1. *The Source of the Photospheric Field*

Photospheric field emerges from deep within the convective envelope in bipolar (active and ephemeral) regions. Emerging bipolar regions are characterized by their flux, their position on the disk, and the orientation of their bipole axis. The numerical model selects these properties at random, based on parent distribution functions. The random sampling approximates the observed histogram of fluxes contained in bipolar regions, the flux-dependent spread in latitude and orientation, and the clustering (or nesting) of active regions (described in § A.1).

Small and ephemeral regions help to populate the parts of the photosphere outside active regions with magnetic field and to maintain flux there where it would otherwise rapidly cancel in collisions between opposite polarities. I therefore include ephemeral regions in the source function describing emerging bipolar regions.

The frequency histogram for the areas of emerging bipolar regions is approximated by a sum of two power laws (eq. [A1]); one power law approximates the active region ensemble, the other is a crude approximation to the poorly known flux histogram for ephemeral regions. Observations of the Sun suggest that the power-law index for the active region population does not change through the cycle. Consequently, I assume for stars of different activity that the power-law indices for both components are fixed. Only the constants of proportionality change with activity. Solar observations show that the cycle amplitudes for active regions and for ephemeral regions differ substantially. This study approximates that difference as follows: if the parameter $\mathscr{A}$ is the constant of proportionality for the population of large active regions (normalized so that $\mathscr{A} = 1$ is typical for a solar maximum), then the number of small ephemeral regions is proportional to $\mathscr{A}^{\alpha}$, with $\alpha = \frac{1}{3}$; the cycle amplitude of a factor of 8 in the active region frequency then translates into the observed amplitude of a factor of 2 for the ephemeral regions.

The areas of the bipolar regions are transformed into fluxes by assuming an average absolute magnetic flux density of 180 G (see § A.1).

2.2. *Transport of Magnetic Field*

Some time after the flux in a bipolar region has fully emerged, the region decays, and its flux disperses across the surface. The large-scale patterns in the solar photospheric field have been successfully modeled by a passive dispersal of a scalar representing the magnetic field (see, e.g., Sheeley, Nash, & Young 1987), even if only the largest 12% or so of active regions are included (Sheeley 1992). The dispersal of magnetic flux in the solar photosphere on large length scales and timescales is consequently modeled as a passive random walk diffusion, in which supergranulation, meridional flow, and differential rotation are involved (see, e.g., Sheeley et al. 1983; DeVore 1987; Wang, Nash, & Sheeley 1989; Sheeley 1992). The details of the largest scale flows and of the supergranular stepping are described in §§ A.2 and A.3, respectively.

To model other stars, the differential rotation can in principle be modified, although stellar data do not appear to require a substantial change. Stellar differential rotation can be measured indirectly by analyzing the spread in short-term modulation periods over many years, or by Doppler imaging of spotted stars (see, e.g., Hall 1991; Donahue, Dobson, & Baliunas 1997). The results suggest that the magnitude of the differential rotation is largely independent of the stellar rotation rate: the shearing timescale, that is, the difference of a full revolution between pole and equator, is only a weak function of rotation rate for stars with Rossby numbers ranging over a factor of 200 (see Schrijver & Zwaan 2000 and references therein; see also Kitchatinov & Rüdiger 1999 for theoretical arguments). The solar profile (in eq. [A3]) is therefore used in most simulations of stars of different levels of activity in this study.

2.3. *Flux-dependent Dispersal and Magnetoconvective Coupling*

A problem for the modeling of the outer atmospheric emissions is that the classical model does not describe the evolution of young bipolar regions before their decay into the supergranular network of mixed polarity field. A curious property of mature active regions is that the average flux density within a fairly well-defined perimeter, excluding spots and pores, averages around 100–150 G, regardless of the region's age or size (Schrijver & Harvey 1994); this is referred to as the plage state. This property is clearly incompatible with a classical random walk dispersal of the field (Schrijver 1989). Apparently, magnetic flux in plages is somehow constrained in its dispersal (see also Worden & Harvey 2000), probably as a consequence of an interaction between the near-surface convection and the magnetic fields.

Solar observations show that larger flux concentrations (which occur predominantly in magnetic plages) tend to disperse more slowly than smaller ones (see § A.3). This tendency is likely caused by the back reaction of the field on the flows, i.e., by the magnetoconvective coupling; this coupling is particularly important for the initial plage decay. The classical random walk diffusion model is modified to incorporate this empirical trend in two alternative ways: (1) a simple two-phase model in which the flux dispersal coefficient is lowered inside magnetic plages relative to the surroundings, using the observed average difference; and (2) a flux-dependent dispersal in which larger concentrations are more sluggish than smaller ones, using an exponential fit to the observed velocity distribution (see § A.3; see Worden & Harvey 2000 for an alternative parametrization of that coupling). The second description is in closer agreement with the observations and, as it turns out, with the observed field patterns on the solar surface.

The flux-dependent field dispersal as used in this study also has an effect on flux dispersal outside magnetic plages. That brings us to a long-standing problem: whereas the classical diffusion model is remarkably successful in describing the large-scale field, the required flux dispersal coefficient of approximately 600 ± 200 km^2 s^{-1} is substantially larger than that derived from the tracking of flux concentrations. The magnetoconvective coupling discussed here slows the larger concentrations that are typically used in tracking studies. This may be the origin of the discrepancy; for an earlier discussion of this possibility, see Schrijver et al. (1996) and also Hagenaar et al. (1999).

The consequences of the flux-dependent dispersal on plage decay and on the large-scale distribution of the field are discussed in § 3.

2.4. *Ephemeral Regions and Small Scales*

In order to use the model to simulate the magnetic field on stars of very different levels of activity, the model should describe the full range of length scales. Therefore, the classical model is modified to include the small and ephemeral regions that populate the mixed polarity network as mentioned in § 2.1. Without this modification, the model would underestimate the flux outside plages by up to an order of magnitude (Schrijver et al. 1998).

In addition to this change in the source flux spectrum, the classical flux dispersal model is also expanded to allow small-scale polarity mixing. To that end, the low-resolution diffusion approximation is replaced by an "atomic" description of small-scale processes. This requires two deviations from the classical model: (1) the spatial resolution needs to be much higher and (2) the interaction of individual concentrations needs to be modeled. The latter is done by including the recipes for fragmentation and collisions of flux concentrations in response to (near-)surface convection as derived by Schrijver et al. (1997a, 1997b). These recipes were demonstrated to describe quiet Sun and magnetic plage alike (§ A.4). The resolution problem is addressed by dropping grids altogether and tracking each concentration individually.

2.5. *Flux Disappearance*

Flux disappears from the photosphere in cancellation collisions: whenever two concentrations come close enough together, the minority species disappears, leaving a residual of the largest concentration behind. The parameters governing this process are derived from a statistical model of the quiet-Sun network, as described in § A.4.

2.6. *The Present Model Compared to the Classical Model*

In summary, to enable the solar-stellar comparison that the present paper aims for, three properties of the photospheric magnetic field are incorporated into a diffusion model for the first time: (1) the flux is modeled by an ensemble of concentrations, subject to collisions and fragmentation; (2) the ensemble of ephemeral regions is included to account properly for emissions from mixed polarity regions on the stellar disk; and (3) a flux-dependent field dispersal is introduced to model the initial decay of active regions. The latter is a fundamental change of the model that turns the linear random walk description of Fickean diffusion into a nonlinear model for flux transport and dispersal.

3. SIMULATING THE SOLAR MAGNETIC FIELD ON ALL SCALES

Figure 1 shows an example of a full-disk magnetogram for a model with standard solar parameters for flux transport and dispersal as discussed in § 2 and Appendix A (listed as run 7 in Table 1), with a flux-dependent random walk dispersal (according to eq. [A5]) for a star characteristic of average solar activity (flux injection parameter $\mathscr{A} = 0.3$). The image shows some of the characteristic poleward arcs of unipolar regions formed by decayed active regions, a still coherent active region, and mixed polarity quiet Sun. The visual impression of the distribution of flux across the solar surface compares favorably with actual solar magnetograms.

A first-order quantitative test for activity levels spanning the solar cycle also turns out satisfactory. For the simulation of the inactive Sun (with $\mathscr{A} = 0.1$; run 6), average Sun ($\mathscr{A} = 0.3$; run 7), and active Sun ($\mathscr{A} = 1$; run 1) the average total absolute flux on the disk in the simulations in KPNO-style synoptic maps is $\approx 2.8 \times 10^{23}$, $\approx 4.8 \times 10^{23}$, and $\approx 1.0 \times 10^{24}$ Mx, respectively. These values agree to within $\approx 10\%$ with the flux in the solar synoptic maps at those phases of the cycle (e.g., Harvey 1992).

A more sensitive test of the agreement of model and real Sun is whether the histogram of flux densities across the surface matches that observed on the Sun. A resolution of 1 deg^2 in heliocentric coordinates (12,000 km at the solar equator) allows comparison to histograms of flux densities derived from solar synoptic maps. To reduce the statistical fluctuations, averages of sets of six synoptic solar magneto-

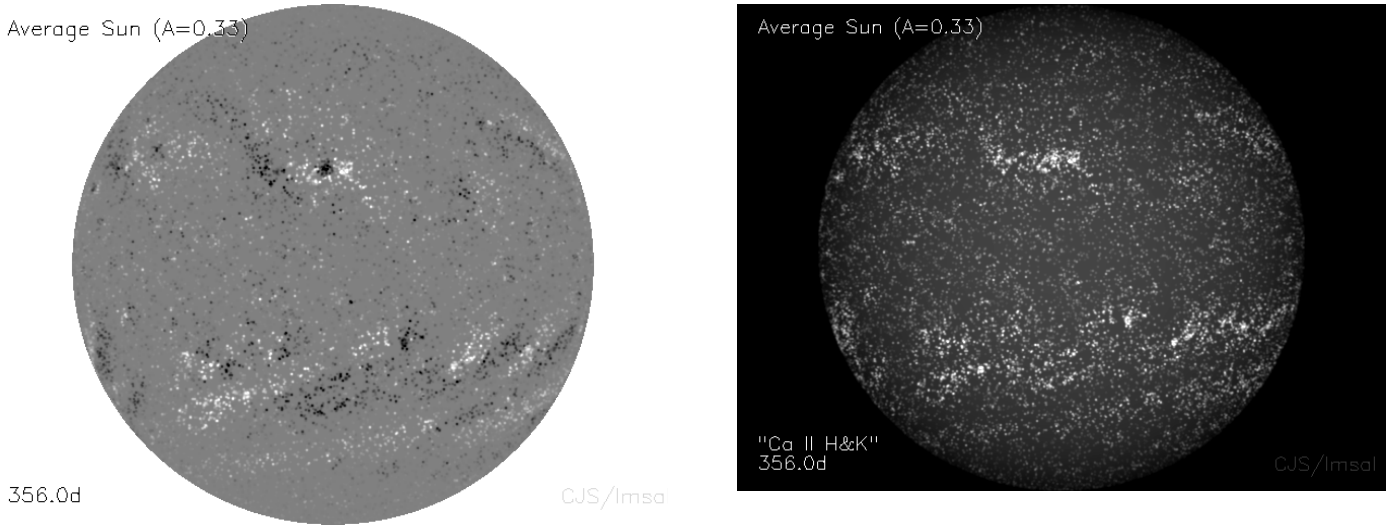

FIG. 1.—*Top:* Sample full-disk magnetogram for the average Sun based on simulations with the standard model (run 7 in Table 1). The simulated disk has subsequently been subjected to a smearing with a Gaussian with FWHM of 5600 km to reflect the fact that most flux concentrations are extended structures comprising a cluster of smaller concentrations, as well as to accommodate some instrumental resolution and/or atmospheric seeing. *Bottom:* Simulated chromospheric image, using a power-law index of 0.6 for the scaling from magnetic to radiative flux density as in eq. (3), plus a weak cos (θ) background to mimic some photospheric contamination or basal contribution.

TABLE 1

MODEL RUNS

Run	$\mathscr{A}$	t (days)	m	d	D (km^{2}s^{-1})	Dispersal Mode	Φ_+ (10^{20} Mx)
Standard Model							
1.....	1	360	1	1	300	2	150
2.....	10^{-5}	360	1	1	300	2	150
3.....	10^{-4}	360	1	1	300	2	150
4.....	10^{-3}	360	1	1	300	2	150
5.....	10^{-2}	360	1	1	300	2	150
6.....	0.1	360	1	1	300	2	150
7.....	0.3	360	1	1	300	2	150
8.....	3	240	1	1	300	2	150
9.....	10	180	1	1	300	2	150
10.....	30	120	1	1	300	2	150
11.....	50	120	1	1	300	2	150
12.....	100	120	1	1	300	2	150
Modified Flux Transport							
13.....	1	360	1	1	300	0	150
14.....	1	360	1	1	300	1	150
15.....	1	360	0	1	300	2	150
16.....	1	240	10	1	300	2	150
17.....	1	360	1	0	300	2	150
Modified Flux Dispersal Coefficient							
18.....	1	360	1	1	600	0	150
19.....	1	360	1	1	150	0	150
Modified Source Functions							
20.....	1	90	1	1	300	2	25
21.....	1	90	1	1	300	2	5

NOTE.—Listed are the run number, flux input parameter $\mathscr{A}$ relative to a very active Sun as defined in eq. (A1), total run time t, multipliers m and d for meridional flow and differential rotation as in eqs. (A2) and (A3), flux dispersal coefficient D, mode of flux dispersal (0: fixed step length; 1: two-phase model differentiating between plage and surroundings; 2: step size dependent on the flux; eq. [A4]), and maximum flux Φ_+ in emerging regions.

grams are used, as computed by Schrijver & Harvey (1989). Note that pixels in a synoptic map, with 1° resolution in longitude and 1/90 in sine latitude, all have nearly equal areas.

This comparison requires that the synoptic maps for the simulated magnetograms are generated in approximately the same way as the solar maps because the time averaging that is involved distorts the flux histograms. The recipe for standard KPNO synoptic maps is the following: take magnetograms for consecutive days and produce a weighted average magnetogram with weights $\cos^4(\varphi_r(t))$, where $\varphi_r(t)$ is the angle over which rotation shifted the surface at the Carrington rotation rate (set to 0 in the simulations). Note that there is no correction for the differential part of the rotation.

In making the synoptic maps from simulations, all pixels are given a noise signal drawn from a Gaussian distribution with a standard deviation of 2 G. Adding this noise improves the agreement between the flux density histograms for the lowest flux densities and could be associated with instrumental noise or the residual signal of intrinsically weak fields in the solar photosphere or both.

This recipe to mimic real-Sun synoptic maps results in a close match between observed and simulated flux density histograms. Figure 2 shows that the flux density histogram for the standard model lies within $\sim$5% of the solar histograms over a factor of 10,000 in relative frequency for conditions comparable to a solar cycle maximum ($\mathscr{A} = 1$).

The simulations for a star with a flux emergence parameter $\mathscr{A} = 0.1$ deviate by up to $\sim$50% if the high-frequency statistically insignificant ripples are smoothed over. This simulation proves to be somewhat too active where the plage component is concerned. The emerging-region counts listed by Harvey (1993) for 1975 May and 1980 September, roughly matching the periods for which the histograms were computed, differ by a factor of 8.8; after she applies corrections for visibility and completeness of the sample, that ratio is 14.4. Given the uncertainty in the visibility/

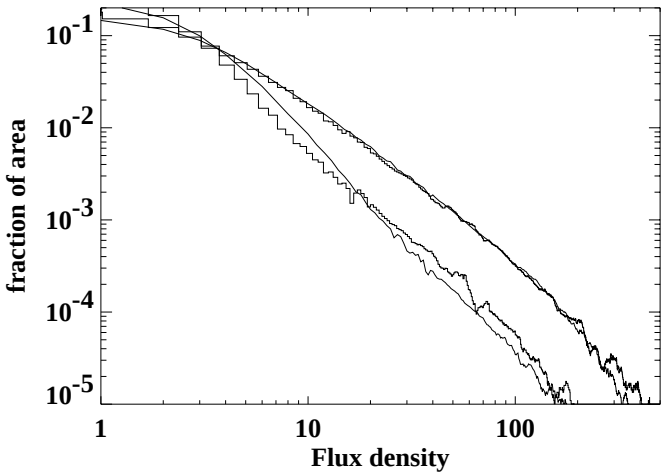

FIG. 2.—Flux density histograms showing the observed solar flux density (in Mx cm^{-2}) histograms (*solid curves*) for cycle minimum (early 1975; average over Carrington rotations 1651–1656) and maximum (late 1980; average over Carrington rotations 1699–1704), constructed as described in § 3. Also shown are histograms for realizations of the standard model simulation (as histograms) for $\mathscr{A} = 1$ (run 1 in Table 1) and $\mathscr{A} = 0.1$ (run 6) . The histograms have been boxcar-smoothed over 10 G intervals above 50 G.

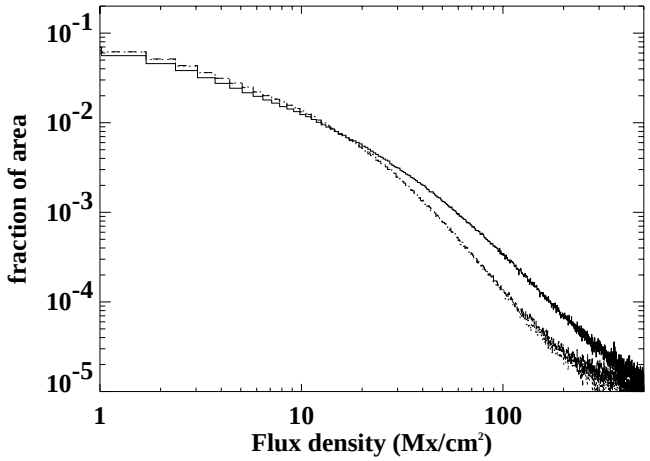

FIG. 3.—Flux histograms comparing three simulations made with a constant step size for all concentrations (*dotted histogram*; run 13 in Table 1), a two-phase diffusion constant (*dashed histogram*; run 14), and a flux-dependent step size (*solid thick histogram*, highest at high flux densities; run 1, also shown in Fig. 3, but there with the temporal averaging used in the construction of synoptic maps).

completeness correction, a ratio of 10 was adopted for the present simulations. Lowering the flux input rate for the cycle minimum simulation by raising the cycle amplitude to a factor of ~ 14 would lower the high flux density tail of the histogram by approximately 40%, which would result in a very good match with the observed flux distribution. The agreement between the simulation and the real Sun is clearly close enough to fall within the uncertainties related to the details of the correction functions for solar observations and the effects of statistical fluctuations in small samples.

That same simulation for $\mathscr{A} = 0.1$ is somewhat less active than the observed distribution below ~ 20 G. This could be solved by either more ephemeral regions, or a larger contribution of small active regions, or perhaps a reduced nesting of active regions. The uncertainties in the cycle modulation for the number of ephemeral regions and for the shape of the flux spectrum are, in fact, substantial (H. J. Hagenaar & K. L. Harvey 2000, private communication), so that I do not attempt a better fit for these simulations.

The differences between the simulations and the real Sun throughout the sunspot cycle are small enough compared to the uncertainties in the source function for solar bipolar regions to have confidence in the model when simulating other stars.

The recipe for the generation of KPNO-style synoptic maps modifies the flux histograms because of the time averaging. This particularly affects the lower end of the distribution functions because of the rapid flux replacement and relatively rapid displacement of the concentrations (cf. Figs. 2 and 3). The primary effect of the temporal smoothing is that the peak at 0 G is effectively smoothed out over the range up to ~ 10 G. The radiative losses from stellar outer atmospheres, which are discussed in § 6, are determined by the instantaneous distribution of fluxes rather than by a time average such as in the synoptic maps. The remainder of this study therefore does not apply time-weighted averaging as in true synoptic maps but averages histograms of fluxes determined at the resolution of standard synoptic maps.

The agreement of the current standard model characteristic of the Sun also implies that the source function for bipolar regions (§ A.1) is apparently approximated adequately from ephemeral regions through large active regions. If regions smaller than 2 deg^2, or $\sim 4.4 \times 10^{22}$ Mx, are excluded from the simulations, for example, the distribution function fails to match observations below approximately 40–50 G, which is almost anywhere outside the plage contours. The relative difference between the standard model and that which excludes small regions increases toward lower flux densities.

The high flux density tail of the histogram of flux densities is dominated by the magnetic plages and their decay products. The active region decay in the model is governed by the flux-dependent field dispersal and by the recipe for the fragmentation of flux concentrations (§§ A.3 and A.4). If a flux-independent flux dispersal coefficient (i.e., a real diffusion coefficient) is used instead as in the classical flux dispersal model (resulting in a linear, Fickean diffusion), then the plages and unipolar areas decay too quickly, resulting in a lower histogram between 20 and 200 G (Fig. 3). The difference in total flux in the low-resolution maps is approximately 33%. That difference and the difference between observed and simulated flux density histograms are so large that this is not acceptable as a solar model.

Another test was for a model in which the flux dispersal coefficient in plages was lowered to 44% of its quiet-Sun value to reflect the average difference between network and plage, regardless of the flux in the concentrations (see the first paragraph of § A.3). This run shows little difference with the classical model with a single, fixed flux dispersal coefficient. Lowering the flux dispersal coefficient from 600 to 150 km s^{-2} for all concentrations (Fig. 4), as an extreme example, raises the entire distribution (except at 0 G, of course). Even such an extreme reduction of the flux dispersal coefficient everywhere to a value that is only observed within magnetic plages does not reproduce the observed flux density histograms. In view of this, I adopt the observed flux-dependent mobility of flux concentrations (as approximated by eqs. [A4] and [A5], with $D = 300$ km^2 s^{-1}) as the best model for the solar magnetic field.

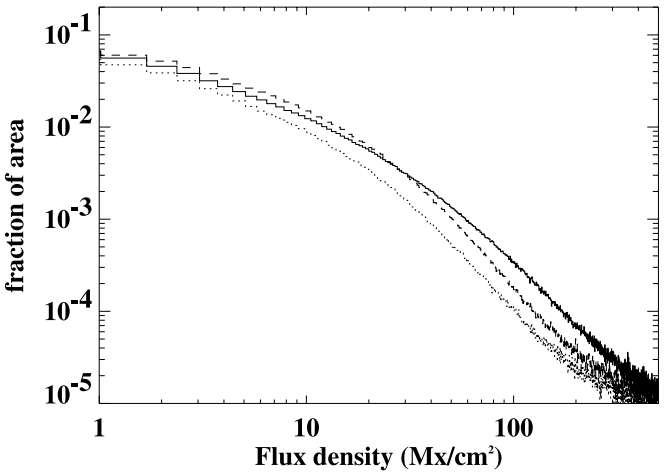

FIG. 4.—Flux density histograms for standard model simulations for average solar activity using three different flux dispersal models: the solid, thick histogram is the standard model (run 1 in Table 1), the dotted curve is for a fixed value of $D = 600$ km^2 s^{-1} (run 18), and the dashed histogram is for a fixed flux dispersal coefficient of 150 km^2 s^{-1} (run 19).

What role do the other parameters play? DeVore (1987) discusses how differential rotation, meridional flow, and random walk dispersal together form the patterns of the poleward arcs of unipolar areas. These are important in the formation and evolution of the low-latitude coronal holes, for example. Yet, it turns out that the surface-integrated flux density histograms in the model computations are only mildly dependent on the magnitude of the differential rotation or whether the meridional flow is comparable to that of the Sun or much weaker (Fig. 5). For a very strong meridional flow, the active regions appear to decay more rapidly, presumably because of the increased shear at midlatitudes.

Tests of the sensitivity of field patterns and flux density histograms to, for example, the details of Joy's rule (the inclination of the bipolar axis relative to the equator), the possible existence of active longitudes, changes in the width of the activity belt, or the possible coexistence of multiple activity belts on the stellar surface are deferred to future studies.

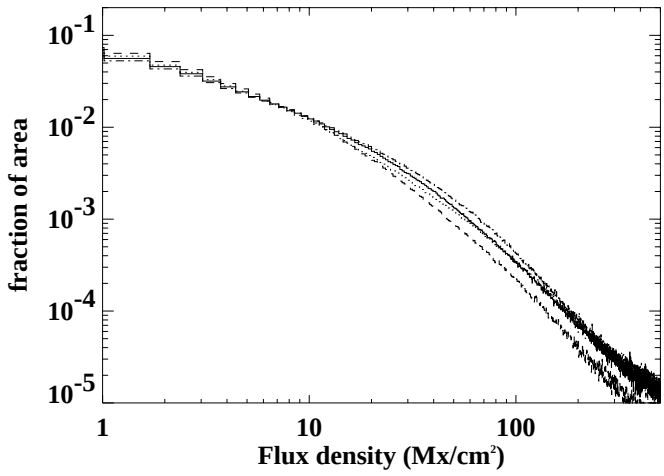

FIG. 5.—Flux density histograms for standard model simulations for a star of average solar activity, but with three different realizations of the largest scale flows: the solid histogram is the standard model (run 1), the dotted histogram (nearly coinciding with that for the standard model) is for zero meridional flow (run 15), the lower dashed histogram is for a meridional flow 10 times stronger than in the Sun (run 16), and the upper dash-dotted histogram is for a model with solid-body rotation only (run 17).

4. MODELING STARS WITH DIFFERENT LEVELS OF MAGNETIC ACTIVITY

The recipes that are used for the simulations of the Sun in § 3 can be used to simulate stars of different activity. As it turns out, stellar data can be simulated adequately by only changing the frequency of emergence of bipolar regions, i.e., by only changing the flux injection parameter $\mathscr{A}$. The results of these simulations are discussed here; some examples of simulations in which other parameters are modified are described in the preceding section, and one more is given at the end of this section.

Figure 6 shows some simulated magnetograms for stars with flux injection rates ranging from 0.1 to 30 times the value of $\langle E_\odot \rangle = 1.2 \times 10^{18}$ Mx s^{-1} for the standard model of the active Sun; the flux input parameter (not proportional to the flux emergence rate; see eq. [A1]) ranges from $\mathscr{A} = 0.01$ to 100. At very low activity levels with $\mathscr{A} \lesssim 0.1$, almost all of the disk is covered merely by the mixed polarity field fed by ephemeral regions; only occasionally does a substantial active region appear, slowly decaying and dispersing on subsequent rotations. For simulations with 0.1–10 times the flux injection rate for the Sun at cycle maximum, the flux patterns are reminiscent of those on the Sun throughout the cycle: active regions, enhanced network, and poleward arcs of unipolar regions dominate different portions of the disks.

For stars with a flux injection rate some 10 times higher than for the active Sun, the active regions form patterns that are only occasionally seen on the Sun: bipolar regions emerge so closely together in space and time that it is difficult to tell which polarity emerged with which on any single magnetogram. For even more active stars, there are increasingly more areas in which the polarities in even substantial active regions are mixed down to very small scales. This is caused by the high rate of emergence of small and ephemeral regions, which counteracts the rapid cancellation of the minority polarity within plage regions so strongly that polarity mixing is clearly observable. The opposite-polarity intrusions are generally small (erased by even moderate spatial smoothing) and short lived (changing from time step to time step). On larger scales, the surface field shows residual active regions, sheared by differential rotation, but the flux density is high almost everywhere, and the typical separation of concentrations is close to the critical radius of 4200 km at which flux concentrations are assumed to coalesce (see § A.4).

The flux density histograms for stars of a range of different activity levels are shown in Figure 7. For the most active stars, the distribution persists out to hundreds of gauss, and there is a larger area coverage at all but the lowest flux densities (at the expense of areas void of flux). The high flux density tail becomes less steep as activity increases. For the solar activity range the tail in the flux density histograms above about 50 G can be approximated by a power law. The associated power-law index is slightly steeper than observed for the Sun (Schrijver 1990). The time averaging involved in the making of solar synoptic maps may be partly responsible for that small difference (compare Fig. 7 to Fig. 2 for solar cycle maximum).

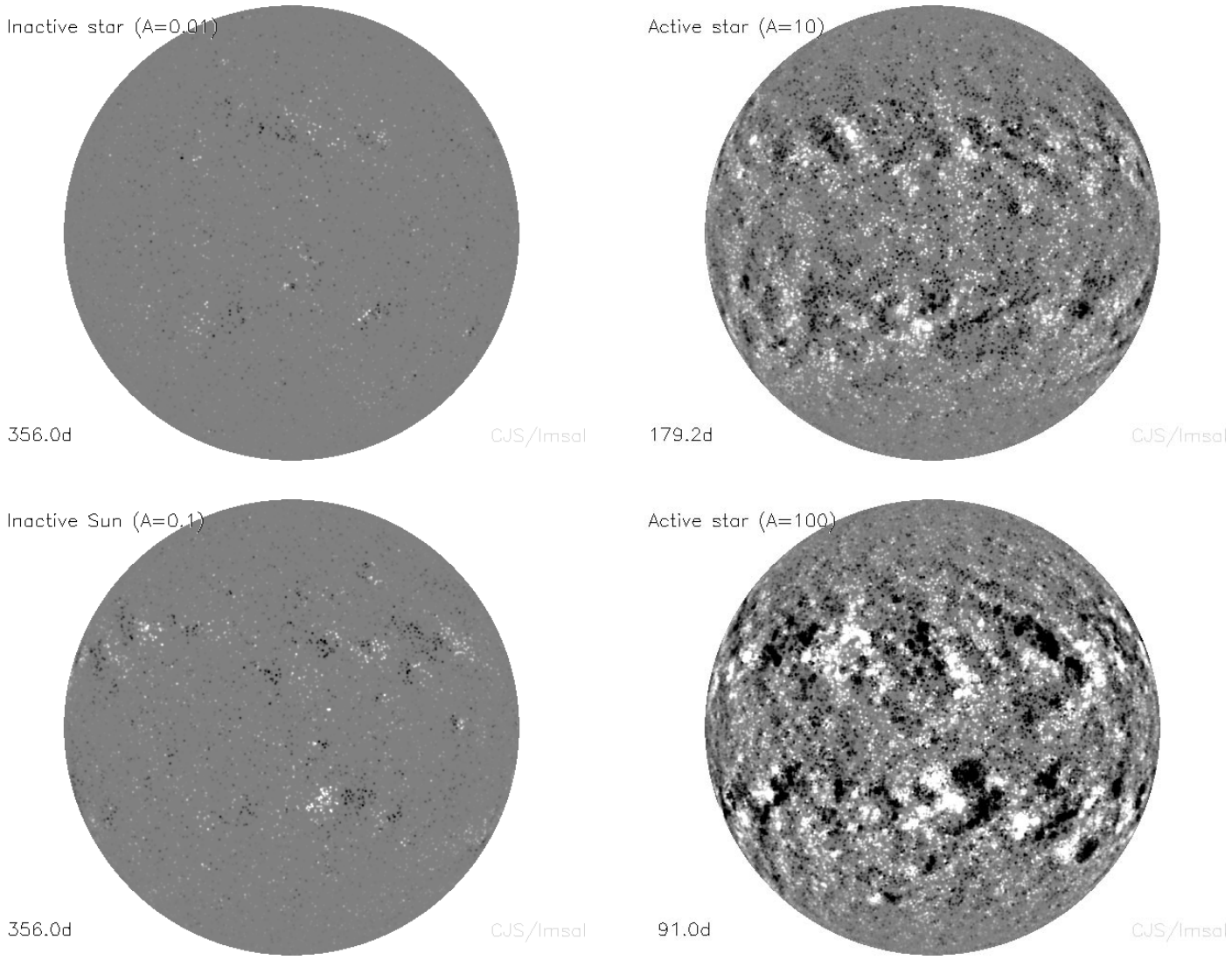

FIG. 6.—Samples of simulated stellar magnetograms for stars that have flux input parameters $\mathscr{A}$ of 10^{-2}, $\frac{1}{10}$, 10, and 100, compared to unity that is characteristic of the active Sun (runs 5, 6, 9, and 12 in Table 1).

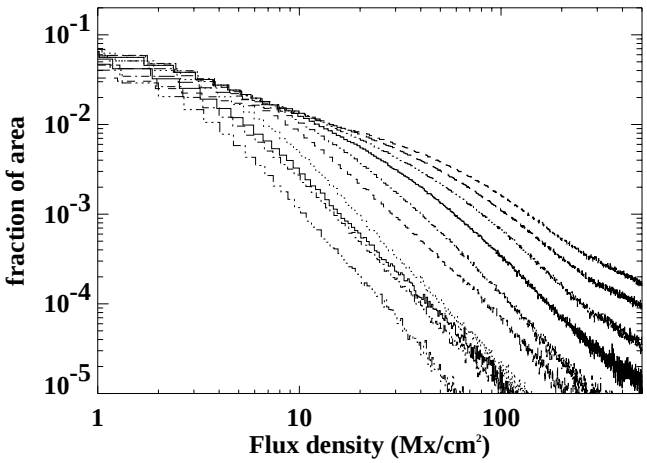

FIG. 7.—Flux density histograms for standard model simulations for a star of different levels of activity, as measured by the rate of flux input into the photosphere. The curves are for flux injection parameter values of $\mathscr{A} = 10^{-5}$ (the lowest at high flux densities), 10^{-4}, 10^{-3}, 10^{-2}, $\frac{1}{10}$, $\frac{1}{3}$, 1, 3, 10, and 30 (the highest at high flux densities); the histograms have been slightly offset horizontally to reduce overlap.

Figure 8 shows an example of what happens to the flux histograms if the source spectrum is truncated at the high end: as the maximum size of the active regions decreases, the high flux density tail of the histograms decreases rapidly as more and more of the photosphere is covered by small concentrations. Such a truncated spectrum may be characteristic of warm stars in which the convective envelope is not deep enough to generate regions substantially exceeding its depth.

5. CALIBRATION OF THE DYNAMO

Stellar magnetic activity involves both the total flux $\langle \Phi_* \rangle$ in the photosphere and the rate of flux emergence (and cancellation) $\langle E_* \rangle$; both of these quantities are important measures of the strength or efficiency of the dynamo process. After all, any dynamo equation models the temporal changes in the field as a function of flows and fields, while there are nonlinear couplings, for example, between the strength of the magnetic field and the magnitude of the α-effect and even the large-scale flows (see Rüdiger & Arlt 1999 for a review). Consequently, establishing the relation-

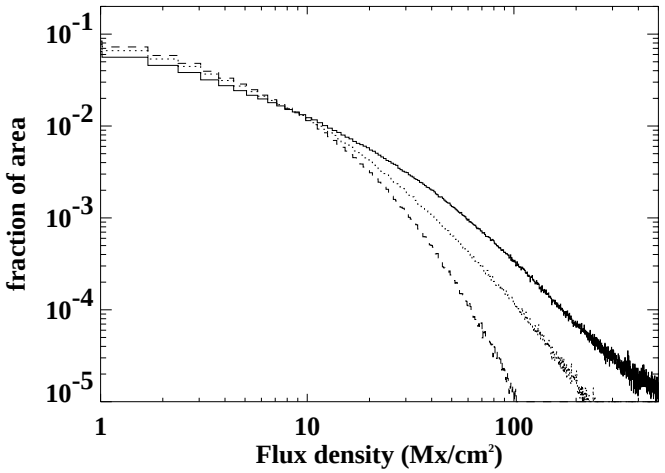

FIG. 8.—Flux density histograms for standard model simulations for a star of average solar activity, but with three different source functions: the solid uppermost histogram is for the full solar spectrum (run 1), the central dotted histogram is for a spectrum excluding regions larger than 2.5×10^{21} Mx (run 20), and the lower dashed histogram is for a spectrum excluding regions larger than 5×10^{20} Mx (run 21).

ship between the total flux present, $\langle \Phi_* \rangle$, and the rate $\langle E_* \rangle$ at which the flux is processed in the photosphere is important to dynamo theory (as well as to the understanding of outer atmospheric heating, discussed in the next section).

The relationship between the flux injection rate and the total amount of flux present in the stellar photosphere (Fig. 9) that results from the present modeling is approximated by

$$\frac{\langle \Phi_* \rangle}{10^{24}} = 0.8 \left(\frac{\langle E_* \rangle}{10^{18}} \right)^{1.01 \pm 0.01}, \quad (1)$$

for $\langle \Phi_* \rangle$ in Mx and $\langle E_* \rangle$ in Mx s^{-1}. This fit is based on the simulations for flux injection rates from 0.2 to ~ 5 times the value at solar maximum. The deviation from this relationship is limited to $\approx 10\%$ throughout this range. Beyond that range, deviations from the fit do not exceed a factor of 2 for the flux injection parameter $\mathscr{A}$ ranging from 10^{-5} to 10^{2} and $\langle \Phi_* \rangle$ ranging over a factor of ~ 500.

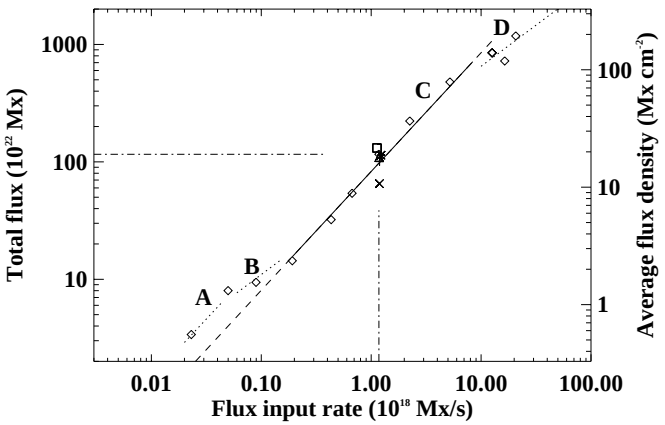

FIG. 9.—Dependence of the total absolute flux (*left-hand axis*) or the surface-averaged absolute flux density (*right-hand axis*) on the rate of flux injection into a stellar photosphere. The diamonds represent the standard model runs (1–12 in Table 1); the dash-dotted line segments identify the standard model for the active Sun (model 1 in Table 1). The power-law fit to the range between 0.2 and 5 times the rate of flux input for an average Sun has a slope of 1.0. The line segment labeling is explained in § 5. Other runs for an active Sun, but with zero meridional flow or 10 times the solar meridional flow, and for a flux-independent flux dispersal coefficient of 200 km^2 s^{-1} nearly coincide with the standard model run for the active Sun. The square shows the result of a simulation with zero differential rotation (run 17); the cross is for a flux-independent flux dispersal coefficient of 600 km^2 s^{-1} (run 18).

The fact that the flux-balance relationship in equation (1) is close to linear is remarkable. The cause of the linearity of equation (1) lies in the difference in cycle amplitude for ephemeral regions and active regions observed for the Sun. In other words, for the simulated stars other than the Sun the cause for the nonlinearity lies in the change of the shape of the flux histogram for emerging regions with activity (as reflected by the differential dependence of the two power-law terms in eq. [A1] on the activity parameter $\mathscr{A}$). Mere numerical cancellation in the case of stationary flux concentrations by continued emergence of flux would yield an expectation value for the flux that increases linearly with the number of local flux injections in the past, but diffusion can modify that. The diffusive evolution of isolated regions would also lead to a linear relationship: each region would evolve largely independently of any others on the disk, and therefore the expectation value of the time-averaged rate of flux cancellation would scale simply with the number of regions and thus linearly with the source strength. Diffusive dispersal within a closely packed environment, however, results in a nonlinear dependence of $\langle \Phi_* \rangle$ on $\langle E_* \rangle$. If, for example, the flux histogram for emerging bipoles were to scale strictly linearly with a multiplier $\mathscr{A}$ (for $\alpha \equiv 1$ in eq. [A1]), the relationship would be a power law with index 0.70. Note that uncertainties in the properties of the ephemeral region properties through the sunspot cycle are substantial enough to make the power-law index in equation (1) uncertain to within some 10%–15%.

With these arguments in mind, the flux balance as shown in Figure 9 can be understood as follows. In the domain of very low activity labeled "A," the few bipolar regions evolve largely independently of each other, resulting in a linear relationship. In the low-activity domain "B" and in the high-activity domain "D," one of the two power-law terms in the flux input spectrum of equation (A1) dominates, resulting in a power-law index of 0.70. Only in the domain "C" of intermediate activity, which contains the Sun throughout the cycle, does the source spectrum change occur in such a way as to result in a linear relationship. We can at present only wonder whether the linearity of the relationship is necessarily how a dynamo regulates its flux budget, or whether it is simply by chance that the function $\langle \Phi_* \rangle \equiv \mathscr{F}(\langle E_* \rangle)$ is linear for a star like the Sun.

6. RELATIONSHIPS BETWEEN OUTER ATMOSPHERIC RADIATIVE LOSSES

The level of activity of a cool star is generally measured by the radiative losses from its outer atmosphere. The measurement of the photospheric magnetic activity of a star presents a more direct measure of the strength of its dynamo, however, because such a quantification circumvents the additional processes of atmospheric heating and radiative and conductive transport of energy. Unfortunately, such measurements are difficult, their interpretation subject to substantial model uncertainties, and the method limited to stars of moderate activity. Hence, the much larger data set of radiative loss measurement constitutes a valuable data set for the study of stellar dynamos.

Interpreting the relationships between the radiative losses is the focus of this section.

One of the most remarkable properties of stellar outer atmospheres involves the relative scaling of radiative losses from the chromosphere, transition region, and corona: if radiative flux densities F_i in individual spectral lines, or in appropriate spectral pass bands, originating from within the outer atmosphere are compared for different stars, these disk-averaged emissions define power laws that extend over more than 4 orders of magnitude in soft X-rays (first pointed out by Ayres, Marstad, & Linsky 1981; Zwaan 1981; Oranje, Zwaan, & Middelkoop 1982). For example, the relationship between the coronal soft X-ray flux density and the chromospheric Ca II H+K flux density above an empirically determined minimal level (that is not associated with strong magnetic fields) is

$$F_{\rm X} \propto F_{\rm Ca\,II}^{1.6\pm0.1} \tag{2}$$

(e.g., Schrijver, Dobson, & Radick 1992), which holds for $F_{\rm X} \approx 7 \times 10^2$–$2 \times 10^7$ ergs cm^{-2} s^{-1}, in other words, over a range of a factor of $\sim$30,000. Rotational modulation, the evolution of the magnetic field, center-to-limb effects, and instrumental and source-related calibration uncertainties result in scatter about these relationships. Within that scatter, the flux-flux relationships appear to be independent of the stellar mass, surface gravity, or effective temperature, at least from mid F-type to mid M-type stars from the main sequence up to bright giants (e.g., Schrijver et al. 1992; Schrijver 1995): once the nonradiative energy reaches the outer atmosphere, the distribution of it over the various domains is apparently largely independent of surface gravity or effective temperature. The observed power-law indices range over a factor of 2 up and down from unity, depending on which two diagnostics are compared.

The nonlinear relative scaling of most radiative flux densities rules out that a stellar outer atmosphere is composed merely of some fixed ensemble of building blocks for which only the frequency differs for stars of different activity. Apparently there is an intrinsic property in the patterns of photospheric magnetic field that introduces a nonlinear relationship between disk-averaged radiative losses by the joint presence of and interaction between its various components.

Even more remarkable than the adherence to power-law relationships between radiative losses from outer atmospheres of most cool stars is that nearly the same power-law relationships are found when observing the Sun with moderate angular resolution (large enough to average over a sufficiently large set of individual structures, but small compared to the Sun's surface area; that moderate resolution should be of the order of 1 deg^2, such as in synoptic maps; see Schrijver 1991, 1992). These transformation properties hold for all radiative diagnostics of outer atmospheric activity, as well as for the absolute magnetic flux density, provided that sunspots are excluded and that the angular resolution is low enough that projection effects between atmospheric field and photospheric sources do not come into play (see the discussion in Harvey & White 1999). The statistical properties of the patterns of the surface magnetic field must be the cause of these transformation properties (Schrijver & Harvey 1989). This entire transformation problem has been the subject of a number of studies, some of which are referenced above; the entire problem is reviewed by Schrijver & Zwaan (2000).

The flux-flux relationships can be used to transform the sample magnetograms in Figures 1 and 6 into their expected chromospheric equivalents, by using

$$F_i = a_i |\phi|^{b_i} , \tag{3}$$

which relates the magnetic flux density $|\phi|$ in the photosphere and the flux density F_i in a radiative diagnostic of activity originating in the outer atmosphere; for a chromospheric diagnostic $b_i \approx 0.6$ (see, e.g., Schrijver et al. 1989). The results are shown in the right-hand panel of Figure 1 and in Figure 10. These images (to which a weak limb-darkened background has been added to show the disk for the least active stars; this background is representative of a photospheric or basal contribution) show that the surface filling in the most active stars is such that the entire disk increases in brightness. The emission in the polar regions is largely due to the many ephemeral regions that emerge at these latitudes because the simulations have not been run long enough to populate the polar caps sufficiently with the decay products of large active regions. In simulations of very active stars, the activity belts stand out in their entirety. The intensity patterns do not reflect active regions as they emerged in the way that we are used to seeing on the Sun because the very high rate of flux emergence causes many new regions to emerge within and near existing regions before these disperse significantly, causing significant flux cancellation between them.

The distributions of magnetic field on the simulated stellar surfaces can be used to study the relationships between disk-averaged radiative flux densities for stars of different activity levels. These flux densities are computed by weighting the expected intensities $I_i(|\phi|)$ from relatively small areas by the appropriate histograms $h_{\rm A}(|\phi|)$ of surface flux densities for different stars. Schrijver & Harvey (1989) performed this experiment for the Sun by using histograms derived from a series of synoptic maps covering an entire activity cycle.

The magnetic flux density, averaged over the stellar surface for some activity level A, is

$$\langle |\phi| \rangle_{\rm A} = \int_0^{|\phi|_{\rm max}} |\phi| h_{\rm A}(|\phi|) d|\phi| . \tag{4}$$

The integration up to $|\phi|_{\rm max}$ excludes sunspots because atmospheric emissions are in general weak over sunspots (the cutoff is also introduced for instrumental reasons; see Schrijver & Harvey 1989). The value of $|\phi|_{\rm max}$ is set to 500 G.

If center-to-limb effects are ignored, the surface-averaged outer atmospheric radiative flux density, $\langle F_i \rangle$, for a local relationship as in equation (3), is approximately

$$\langle F_i \rangle_{\rm A} = \int_0^{|\phi|_{\rm max}} a_i |\phi|^{b_i} h_{\rm A}(|\phi|) d|\phi| . \tag{5}$$

The relationship between $\langle F_i \rangle_{\rm A}$ and $\langle |\phi| \rangle_{\rm A}$ for the Sun throughout the solar cycle, for example, is obtained by performing the integrations in equations (4) and (5) at different phases of the solar cycle. Schrijver & Harvey (1989) find that

$$\langle F_i \rangle_{\rm A} \approx f(b_i) a_i \langle |\phi| \rangle_{\rm A}^{b_i+\delta_i} , \tag{6}$$

where $f(b_i) = 2.5^{b_i(b_i-1)}$ and δ_i is a deviation that is small compared to b_i. If, for example, $b_i = 0.6$, as is the case for the Ca II K line core emission (see above), then $f(b_{\rm CaII}) = 0.80$

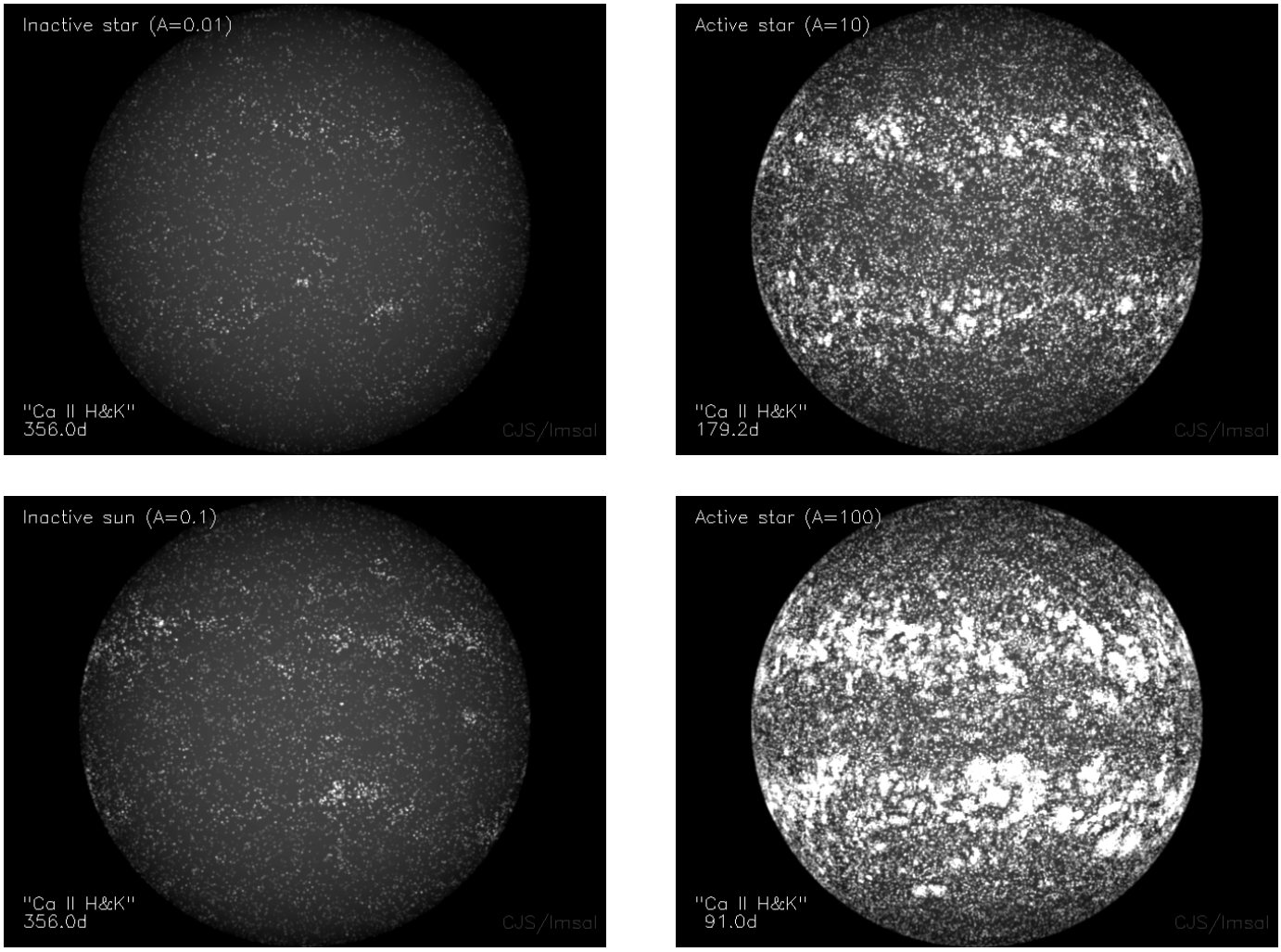

FIG. 10.—Simulated chromospheric images for the simulated magnetograms shown in Fig. 6, using eq. (3) with $b = 0.6$, plus a weak background as in Fig. 1.

and $\delta_i \sim -0.05$ (see Schrijver 1991). This explains the seemingly surprising result that the relationship for mean stellar fluxes and the relationship for solar fluxes with a moderate angular resolution are nearly the same. Note that the observational uncertainties allow that the solar and stellar power-law indices differ by as much as $\delta_i \sim \pm 0.1$. Part of that deviation is now understood from this study, as explained below.

This same exercise in transformations from local to global flux-flux relationships can now be carried out for the models of stars of widely different activity levels. In this study, the surface-averaged signal is computed using a surface average over a 2 month period. The resulting relationships between magnetic and radiative diagnostics (derived using eqs. [4] and [5], for average histograms based on instantaneous field maps at the resolution of synoptic maps, as discussed in § 3) are shown in Figure 11. Within most of the range of the simulations, the results are power laws, with power-law indices near the input values: an index of 0.6 becomes 0.71, and 0.8 becomes 0.86.

This study finds that the transformation of power laws based on solar synoptic maps results in slightly different power-law indices and offsets than those based on instantaneous maps. The values of the power-law indices for the disk-integrated properties are spuriously closer to the input values for the synoptic maps (*triangles* in Fig. 11). This is an artifact of the time averaging involved in the making of synoptic maps as is easily demonstrated with the model results: using the recipe for true synoptic maps for the flux-flux transformations places the simulated results very close to the observational results of Schrijver & Harvey (1989), as shown by the short, thick line segments for the inactive and active Sun in Figure 11.

Apparently, the solar flux injection and dispersal are such that the local and disk-averaged relationships are nearly the same, i.e., the values of δ_i for different diagnostics of activity are small and the values of $f(b_i)$ are not very different from unity. Figure 12 shows that changing the differential rotation or meridional flow has little impact on these scaling properties (as expected from the discussion of the flux histograms in Fig. 5 above): surface-averaged quantities remain near the best fit to within a few percent. Only changing the flux dispersal coefficient or the flux input spectrum has a larger effect (runs 18, 20, and 21 in Table 1), but still the deviation is only some 20%. Apparently, the tight power-law scaling of surface-averaged flux densities is mostly sensitive to the requirement that substantial flux input occurs over most of the stellar surface, scaling roughly with the

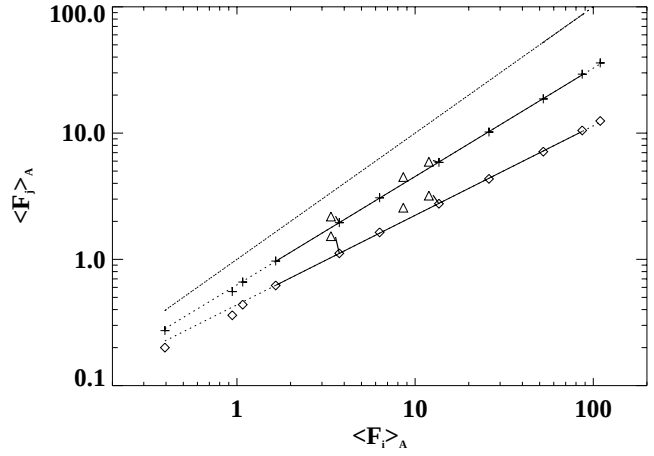

FIG. 11.—Simulations of surface-averaged flux-flux relationships, using instantaneous flux density histograms based on maps with the resolution of KPNO synoptic maps, not including temporal averaging or background noise. The diamonds and asterisks are for power-law indices in eq. (3) of 0.60 and 0.80, respectively; the power-law fits (to the points within the domain of the solid line segments) have slopes of 0.71 and 0.86, respectively. The triangles show the solar location in the early-rise, mid-rise, and cycle maximum phases based on synoptic (and therefore time-averaged) magnetograms (from Schrijver & Harvey 1989). The thick line segments show the difference for the simulated Sun for $\mathscr{A} = 0.1$ and $\mathscr{A} = 1.0$ between the use of averages of instantaneous maps of the field (*lower end point*) and synoptic maps that involve time averaging (*upper end point*). The dotted line represents the identity relationship that would result from a linear relationship between spatially resolved data.

mean activity level. Establishing the constraint that this puts on activity patterns on stars is left to future studies.

7. CONCLUSIONS AND DISCUSSION

This paper presents the first comprehensive simulations of the dynamic photospheric magnetic fields of the Sun and other cool stars and of the surface-averaged radiative losses associated with these fields. The model reproduces the histogram of flux densities for the Sun from very quiet regions to the most active areas across the solar surface with good accuracy throughout the activity cycle. The simulations are successful, provided that three properties of the solar magnetic field are incorporated in the classical surface diffusion model: (1) an "atomic" description of the field that allows small-scale polarity mixing, (2) the ensemble of ephemeral regions and small active regions that contributes significantly to the outer atmospheric emission of a star like the Sun, and (3) magnetoconvective coupling that makes the transport process nonlinear by letting the flux dispersal depend on the flux in the concentrations. None of these properties were incorporated in earlier random walk models that focused exclusively on large-scale field patterns. The combined effect of the newly included processes is likely to explain the traditional mismatch between observed and required flux dispersal coefficients in the classical model: the relatively large mobility of the multitude of small concentrations increases the effective dispersal rate over that inferred from the preferential tracking of the larger ones (as proposed by Schrijver et al. 1996).

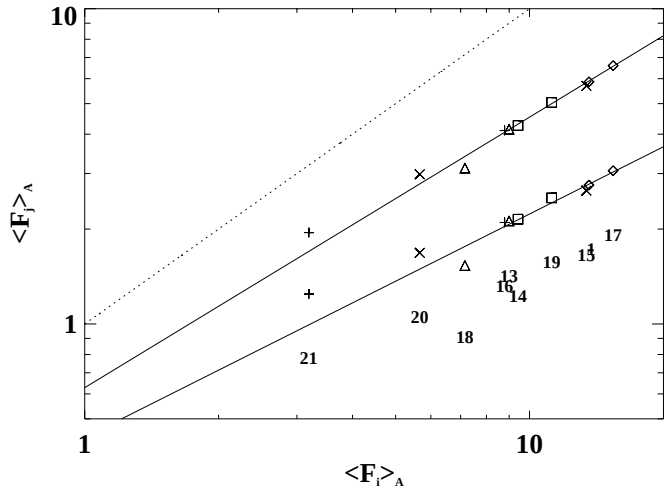

FIG. 12.—Similar to Fig. 11, but for a reduced range of the axes. Shown are the best fits for the standard model from Fig. 11. Symbols show the transformation properties of a set of other simulations, identified below the symbols by numbers as in Table 1.

The simulations reproduce the disk-integrated properties of cool stars that differ in activity by a factor of ≈ 1000 as measured by the rate of flux emergence, $\langle E_* \rangle$, or almost as much in the disk-averaged absolute flux, $\langle \Phi_* \rangle$, in their photospheres. The relationships between simulated disk-averaged absolute magnetic flux density and the expected outer atmospheric radiative flux densities $\langle F_{i,*} \rangle$ in chromospheric, transition region, and coronal diagnostics are close to simple power laws over this entire range of activity levels, in agreement with stellar observations. The simulations show that the differences in power-law indices between locally and globally valid flux-flux relationships are no larger than ~ 0.1 for the observed range, in keeping with solar observations, but holding over a much larger range in activity levels than exhibited by the Sun.

The linearity of the flux-balance relationship of $\langle \Phi_* \rangle \equiv \mathscr{F}(\langle E_* \rangle)$ (eq. [1]) for stars with surface fluxes ranging from $\frac{1}{10}$ to 10 times the value at solar maximum is the result of (1) the diffusive dispersal of magnetic field in an environment where bipolar sources are closely packed and (2) the change in the source function for bipolar regions in which the active regions become relatively more numerous than the ephemeral regions as activity increases. Note that this linearity is the result of using the best available data for the source and dispersal properties of the solar photospheric field; it is not built into the model because there were no fits of free parameters. However, the unknown uncertainties in ephemeral region properties make the power-law index in equation (1) uncertain to within probably no more than 10% given that a more than realistic change in the source spectrum by raising α in equation (A1) from $\frac{1}{3}$ to 1 changes the power-law index by only 30%.

What is the impact of the linear flux-balance relationship on our understanding of the rotation-activity relationship for cool stars? One of the peculiarities of stellar activity is that main-sequence stars of spectral types from early F to mid M, ranging from stars with very shallow convective envelopes to nearly fully convective stars, obey the same relationship

$$R_i = \alpha_i \langle \Phi_* \rangle^{\beta_i} = g_i\left(\frac{P}{\tau_c}\right). \quad (7)$$

In this equation, $R_i \equiv F_i/(\sigma T_{\rm eff}^4)$ is some outer atmospheric radiative flux density normalized to the bolometric flux density. The function g_i depends on the Rossby number, P/τ_c, in which P is the stellar rotation period and τ_c is an empirically determined color-dependent scaling function

that resembles the convective turnover time at the bottom of the convective envelope for a mixing length of two pressure scale heights (see Noyes et al. 1984 for the original study and Schrijver 1993 for an extension to early F-type main-sequence stars). Equation (7) holds for all stars of roughly Sun-like activity and above; the less active stars appear to deviate somewhat (see Schrijver & Zwaan 2000 for a discussion of deviations from the rotation-activity relationship).

The present simulations demonstrate that $\langle \Phi_* \rangle$ is a function of the flux dispersal coefficient D and of the properties of the flux injection. Why do these dependences not show up in equation (7)? On one hand, one could imagine that the supergranular flux dispersal coefficient D (as yet unknown for other stars) varies little along the main sequence. If the source spectrum would also change relatively little with stellar mass, effective temperature, and stellar rotation, then the lack of an observed dependence other than the convective turnover time in equation (7) would be understandable.

On the other hand, a less restrictive and less ad hoc argument can be made that the dependence on D does not show up because of two partially compensating effects. An increase in the flux dispersal coefficient decreases the total flux in the photosphere (Fig. 13*d*). If the outer atmospheric heating scales with the random walk dispersal coefficient D (as expected in the case of field line braiding, and assuming the same comparability between granular and supergranular flux dispersal coefficients as seen on the Sun), then a change in the average absolute flux density in the photosphere by changing D would be counteracted by the change in the atmospheric heating (Fig. 13*c*). This would reduce the dependence of equation (7) on the value of D (Fig. 13*a*). This compensation is unlikely to hold exactly and also probably depends on the details of the flux source (left unchanged in the scenario in Fig. 13), but the resulting deviations might be small compared to the scatter about the mean rotation-activity relationship. If this hypothesis is correct, we may wonder whether the deviation of giant stars from equation (7) is the result of more substantial differences between the properties of the flux source, flux dispersal, and atmospheric heating between dwarf stars and giant stars than exist between stars along the main sequence.

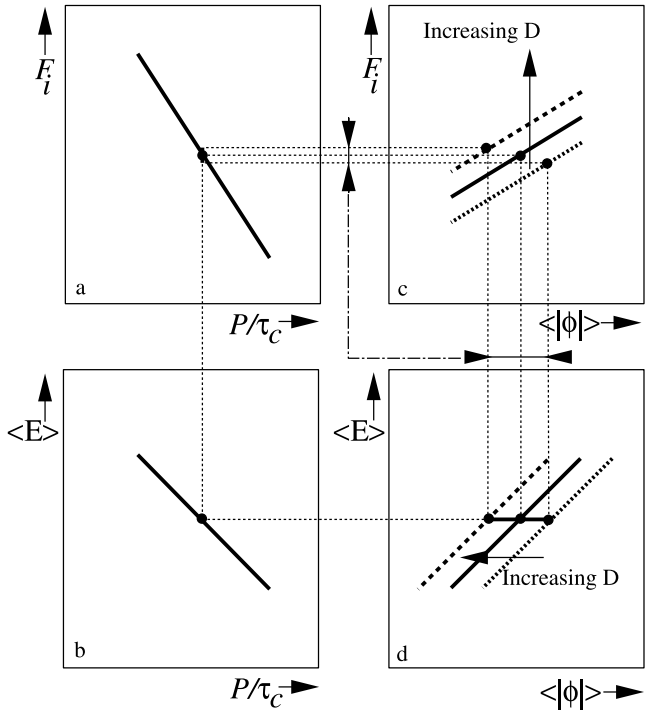

FIG. 13.—Illustration of the relative insensitivity of the flux-flux relationship to the flux dispersal coefficient of magnetic flux in the photosphere: given a Rossby number (panels [*a*] and [*b*]), the flux input rate is determined. The total amount of flux that resides in the photosphere given the flux input rate increases with decreasing flux dispersal coefficient D (panel [*d*]), while braiding-induced heating decreases with decreasing random walk flux dispersal coefficient (panel [*c*]). These counteracting effects reduce the sensitivity of the rotation-activity relationship to D.

The numerical model developed in this paper can also be applied to properties of active stars other than the flux-flux relationships. Consider, for example, the characteristic coronal temperature. As the level of activity of a star increases, the coronal emission is increasingly dominated by the active regions. This is associated with an increase in the characteristic coronal temperature because the active region corona is hotter than the quiet disk corona. This is indeed observed for the Sun (Peres et al. 2000). If activity is increased further, the plages of mature active regions and the patches of still strong but already decaying regions become more and more closely packed. Thus, the outer, high-arching loops of active regions are likely to close to nearby opposite-polarity fields. On the Sun, these long loops are typically cool, at 1–1.5 MK (Schrijver et al. 1999). With their disappearance, even more of the relatively cool coronal material disappears, and the characteristic coronal temperature is expected to increase even further. With the increased frequency of flux emergence and cancellation, the flare frequency is expected to increase (see the discussion by Güdel 1997). All three of these effects raise the characteristic coronal temperature with activity, as is indeed observed for stars (e.g., Schrijver, Mewe, & Walter 1984).

The simulations in this study extend to stars with such large flux injection rates that their surface-averaged flux density reaches 200 G, which is above the average value for a solar active region. The results for these stars are clearly a stretch of the solar characteristics. Some young stars are even more active than that (Saar 1996), however, often with starspots covering substantial fractions of their surfaces, even covering much of their polar caps. Such polar spots are never seen on the Sun and thus appear to require some fundamental change in the dynamo patterns of these stars. These very active stars also fit the flux-flux power-law relationships, despite the fact that the high-latitude or polar cap spots and any associated plages are fundamentally different from the mid- and low-latitude field patterns simulated in this study. Apparently there is an intrinsic nonuniqueness in studies of photospheric fields that rely on disk-integrated radiative losses. Exploring the possible polar cap field patterns with the code developed here requires a substantial increase in computing efficiency, as well as information on the dynamo patterns of very active stars. Establishing the flux source properties for these stars requires some form of imaging of cool star atmospheres.

I thank A. M. Title for discussions and for comments on the manuscript, J. W. and K. L. Harvey and V. Gaizauskas for input on solar processes, and the referees for triggering a substantial change in the presentation of the results. This work was supported by NSF grant ATM 953-1778.

APPENDIX A

A1. SOURCE FUNCTION FOR BIPOLAR REGIONS

The source function of active regions (defined as bipolar regions larger than 2.5 deg^2) has been extensively studied by Harvey & Zwaan (1993) and Harvey (1993). They establish a spectrum of active region areas at maximum development for regions of 2.5 deg^2 and larger: this source function is a monotonically decreasing function of size that varies mostly in amplitude and somewhat in shape throughout the solar cycle. Harvey & Zwaan (1993) also provide information on the latitude distribution and bipole orientation as a function of size. Active regions exhibit a preference for clustering: 40% of active regions emerge within existing magnetic plages, i.e., within regions with an average magnetic flux density that exceeds approximately 50 G when observed at moderate resolution.

The area distribution function $n(S, t)$ of bipolar regions as measured at maximum development has been established by Harvey (1993); see also Harvey & Zwaan (1993) and Zwaan & Harvey (1994). Harvey & Zwaan (1993) apply corrections for incompleteness in the sample and normalize to a number density per hemisphere, per day, per square degree in area S (1 deg^2 is approximately 150 Mm^2). Their sample comprises 978 active regions and 9492 ephemeral regions. They find that the active region spectrum is a power law throughout the cycle, varying mostly in amplitude and little in slope. The ephemeral regions have a substantially lower amplitude throughout the cycle than the active regions. The source function for ephemeral regions (defined as bipolar regions smaller than 2.5 deg^2) is not well established. The combination of simulations in this paper with recent results in the literature and in ongoing research constrains their source function to fair accuracy. The bipolar region source function is approximated by the sum of two power laws:

$$n(S, \mathscr{A})dS\,dt = (a_0\,\mathscr{A}S^{-p} + a_1\,\mathscr{A}^{\alpha}S^{-p-1})dS\,dt\ , \tag{A1}$$

where $\mathscr{A}$ is the flux injection parameter that is varied to simulate stars at different levels of activity. No regions smaller than $\Phi_- \equiv 1.2 \times 10^{19}$ Mx or larger than $\Phi_+ \equiv 1.5 \times 10^{22}$ Mx are injected unless otherwise specified.

The active region spectrum (per hemisphere) at cycle maximum is approximated by $a_0 = 8$ and $p = 1.9$, as determined by a fit to the area distribution for emerging active regions as derived by Zwaan & Harvey (1994). For the ephemeral regions, a steeper spectrum is used to match the slope of the distribution for ephemeral regions as plotted by Zwaan & Harvey (1994). The value of a_1 is set to 8 deg^{-2} day^{-1} hemisphere^{-1} in order to match the total flux input, as explained below. The weaker cycle dependence for the ephemeral region frequency compared to the active region frequency, as found by Harvey (1993), is approximated through a power-law scaling with the flux emergence parameter $\mathscr{A}$ with a power-law index $\alpha = \frac{1}{3}$.

The rate of flux input in ephemeral regions is still being investigated. H. J. Hagenaar (2000, private communication) finds a range of $\approx$(5–10) $\times 10^{17}$ Mx s^{-1} based on *SOHO*/MDI observations. C. Parnell (2000, private communication) estimates the rate to be $\approx 6 \times 10^{17}$ Mx s^{-1} derived from simulations of the dynamics of magnetic flux in the quiet network. Worden & Harvey (2000) apply flux dispersal simulations to synoptic maps and find a value of $\approx 2.5 \times 10^{18}$ Mx s^{-1} for a quiet phase of the cycle; this is likely an overestimate because of numerical cancellation effects in their algorithm, but the magnitude of that effect is not known. Schrijver et al. (1997b) derive a value of (1.5–3) $\times 10^{17}$ Mx s^{-1} for an extremely inactive Sun based on detailed modeling of the flux spectrum in the quiet network. The value of $a_1 = 8$, combined with the lower cutoff flux of 6×10^{18} Mx per polarity and with $\mathscr{A} \approx \frac{1}{8}$ (characteristic of cycle minimum), results in a flux injection rate of $\approx 5 \times 10^{17}$ Mx s^{-1} for a quiet Sun that lies between the values found in the literature.

Note that equation (A1) should not be used to fit the ephemeral region area spectrum as derived by Zwaan & Harvey (1994) for two reasons: (1) mostly because of the breakdown of the proportionality between area and flux for the smallest regions (which is a property that has not yet been studied) and (2) to some extent because of uncertainties introduced by the low observing frequency of the magnetograms analyzed by Harvey.

The distribution in latitude of emerging bipolar regions centers on an average latitude that shifts toward the equator as the solar cycle progresses. Bipolar regions of all sizes show the same average latitude, but the spread about the mean increases with decreasing size. We use the diagrams published by Harvey (1993) on the latitude distribution as a function of active region size to approximate the scatter about the mean latitude as a Gaussian distribution with a standard deviation of $\sigma_\theta(\theta - \bar{\theta}) = \theta_0 \exp(-\Phi/\Phi_\theta) + \theta_1$, for $\Phi_\theta \approx 5 \times 10^{20}$ Mx, $\theta_0 \approx 25°$, and $\theta_1 \approx 4°$. The average latitude is set to $\bar{\theta} = 17.°5$ in all simulations, neglecting associated cycle-related effects. Bipolar regions are assigned an equal probability to emerge on either hemisphere.

Harvey & Zwaan (1993) demonstrate that bipolar regions have a preference to emerge at locations where flux emerged before, thus forming active region nests. They find that approximately 40% of all active regions emerge within the boundaries of existing magnetic regions, while the area distributions for regions emerging inside and outside existing magnetic plage are not significantly different. Consequently, the longitude distribution of the emerging flux regions in the model is chosen such that 60% of them are assigned a random longitude selected from a uniform distribution, while 40% emerge within magnetic plage as determined from the synoptic map described in § A.3. All pixels within magnetic plages have an equal probability of becoming the central site for a new region to emerge.

Each region is given a dipole orientation that is inclined relative to the equator according to Joy's rule. Harvey (1993) demonstrated that the spread about the average inclination increases with decreasing size. The present simulation uses the following approximation for the standard deviation of the Gaussian distribution of the deviation from the mean: $\sigma_\iota(\iota - \bar{\iota}) = \iota_0 \exp(-\Phi/\Phi_\iota) + \iota_1$ for $\Phi_\iota \approx 8 \times 10^{19}$ Mx, $\iota_0 \approx 90°$, and $\iota_1 \approx 18°$. The average inclination is set to $\bar{\iota} = 4.°2$ (the average value for the entire sample; Howard 1991). The orientations on the two hemispheres match the Hale-Nicholson polarity law while allowing regions of opposite orientation to exist in accordance with the scatter about the mean inclination. This approximation ignores the slightly enhanced probability for orientations opposite to the most likely one.

The model does not attempt to mimic the initial emergence phase: flux is injected instantaneously, partitioned into concentrations with typically 1.5×10^{19} Mx each; for regions with less than 4.5×10^{19} Mx per polarity, the flux is distributed over three concentrations with one-third of the flux each, crudely mimicking observed ephemeral regions. The fluxes are given a spread by adding a number drawn from a Gaussian probability distribution centered on 0 with a width equal to the square root of the mean value.

The concentrations are positioned at randomly selected positions that are distributed uniformly in radius and position angle (this concentrates flux toward the center of the polarity domain, reflecting the presence of spots in young active regions) within two circular areas such that the mean flux density is 180 G; this value is higher than that characteristic of the plage state described in § 1, correcting for the approximation that roughly 20% of the flux resides in dark spots and pores. The circular areas for the two polarities are positioned such that they touch for large regions but have a minimum separation of their centers of 18,000 km to simulate the initial separation of polarities of ephemeral regions by the supergranular flow. The circular area is never smaller than 7000 km, in keeping with ephemeral region appearance, which shows the polarities broken up into a few concentrations in a small cluster.

A2. DIFFERENTIAL ROTATION AND MERIDIONAL FLOW

The meridional flow in all simulations is approximated by

$$M(\theta) = m[12.9 \sin(2\theta) + 1.4 \sin(4\theta)] \quad (\mathrm{m\ s^{-1}}) \tag{A2}$$

(Komm et al. 1993b), with multiplier $m = 1$ except where explicitly stated otherwise (see Table 1).

The differential rotation profile is taken from Komm et al. (1993a) as derived from cross-correlation analyses of Kitt Peak magnetograms:

$$\Omega(\theta) = d[\Omega_0 - 1.95 \sin^2(\theta) - 2.17 \sin^4(\theta)] \quad (\mathrm{deg\ day^{-1}}) , \tag{A3}$$

with multiplier $d = 1$ except where stated otherwise (see Table 1). The value of Ω_0 is irrelevant for the present model computations.

A3. DISPERSAL OF FLUX AND MAGNETOCONVECTIVE COUPLING

In each time step, all flux concentrations are moved in a random direction on a sphere, with a step length that is determined by the characteristic flux dispersal coefficient D and the time step Δt:

$$\Delta r = C(|\Phi|)\sqrt{4D(|\varphi|)\Delta t} , \tag{A4}$$

where Φ is the flux contained in the concentration and φ is the average flux density in the neighborhood of the concentration. The flux dispersal coefficient $D(|\varphi|)$ may depend on the local average flux density $|\varphi|$. Such a dependence was observed in the study by Schrijver & Martin (1990): they estimate $D \approx 250$ km s^{-2} in a quiet region surrounding a magnetic plage and 110 km s^{-2} in the magnetic plage itself. In some simulations, D is therefore approximated by a step function (see Table 1); in most cases, however, D is taken to be a constant. The function $C(|\Phi|)$ introduces a magnetoconvective coupling that is described later in this section.

For the purpose of this study, magnetic plages and their nonplage ("quiet") complement are defined using the local average flux density. The first step toward this distinction is the construction of a latitude-longitude chart of the absolute flux density with a resolution of 1° in longitude and 1/90 in sine latitude (the resolution used in standard Kitt Peak synoptic maps to enable comparison with the study by Schrijver & Harvey 1989; see below; note that the pixels in these maps have nearly equal areas). A 40 G threshold is then imposed to determine the plage perimeter; this is somewhat lower than the value of 50 G established by Schrijver (1987) to compensate for the lower resolution in the charts used here compared to the full-disk magnetogram used in that study. A new map is then generated in which all pixels with six or more neighboring pixels exceeding the threshold are set to unity. That map is subsequently dilated with a 3×3 kernel to add a ring of 1 pixel wide to the bitmap. This same definition of "magnetic plage" is used to simulate the clustering of active regions, as discussed in § A.1.

Studies by Schrijver et al. (1996) and Hagenaar et al. (1999) establish a trend for a diminishing displacement velocity with increasing flux in the concentration. This trend is parametrized here as an exponential relationship:

$$C(|\Phi|) = 1.7 \exp\left(\frac{-|\Phi|}{3 \times 10^{19}}\right) \tag{A5}$$

(all fluxes in Mx). Schrijver et al. (1996) argue that this trend in the mobility of flux concentrations might explain why observed values of the flux dispersal coefficient are too low to be compatible with the classical diffusion model and also why diffusion in plages is slower than in active regions. It is not known in detail how this dependence affects the flux dispersal coefficient; for the purpose of this study, the approximation in equation (A4) is used in the "standard model" for $C(|\Phi|)$ as given by equation (A5), although some nonstandard model simulations are made with $C(\Phi) \equiv 1$ (see Table 1).

A4. COLLISIONS BETWEEN AND FRAGMENTATION OF FLUX CONCENTRATIONS

After every step, all concentrations within a certain distance from a particular concentration are assumed to coalesce into a single source. The resulting concentration is placed at the location of one of the concentrations involved; that concentration is selected randomly from the colliding set. The critical distance is derived from the collision frequency ν derived by Schrijver et al. (1997b), who argue that the total number of collisions per unit area per unit time in very quiet Sun equals $\nu = \lambda v n^2$ km^{-2} s^{-1} for a concentration density n (km^{-2}), an average displacement velocity v (km s^{-1}), and a mean-free path length λ (km);

they derive a collision frequency corresponding to $\lambda v = 1400$. For an average horizontal displacement velocity for concentrations of $v = 0.3$ km s^{-1} (Simon, Title, & Weiss 1995), the critical distance, or mean-free path in quiet network, is $\lambda = 1400/v = 4200$ km. All concentrations are assumed to be point sources.

The statistical model developed by Schrijver et al. (1997b) uses a fragmentation probability for flux concentrations that is proportional to their flux. The distribution functions of fluxes in quiet Sun and in a magnetic plage suggest that this holds for concentrations with fluxes up to at least 1.5×10^{20} Mx (see also Schrijver et al. 1997a). Larger concentrations that form large pores or sunspots are observed to live for a number of days. In order to incorporate this in the model in an approximate way, the following fragmentation probability (per second) is used:

$$P(\Phi)dt = k_0 \Phi \left[0.008 + \exp\left(\frac{-\Phi}{1.2 \times 10^{20}} \right) \right] dt \, , \tag{A6}$$

with $k_0 = 0.6 \times 10^{-6}$ (see the graphic representation in Fig. 14), which introduces a secondary peak to the monotonic lifetime distribution used by Schrijver et al. (1997b). Concentrations are taken to fragment into fractions f and $1 - f$, with f a random number homogeneously distributed between 0 and 1 (as in Schrijver et al. 1997b). The largest of the two fragments remains at the original location; the smaller of the two is displaced over a distance of 5000 km, in a random direction. This constant is sensitive to the details of the flows that separate fragmented flux concentrations, which cannot be determined reliably ab initio because insufficient observational constraints are available. Hence, the value was determined iteratively so that the model for the mixed polarity quiet network on an inactive Sun ($\mathcal{A} = 0.1$) matches the observed exponential distribution of fluxes found by Schrijver et al. (1997b). The separation distance somewhat exceeds the distance for coagulation, as indeed it should.

The modification according to equation (A6) of the proportionality of the fragmentation rate and flux used by Schrijver et al. (1997b) is rather arbitrary. It reflects only crudely the relative stability pores and small spots. The properties of large spots are left for future study. Yet, together with the parametrization of the flux-dependent flux dispersal in equations (A4) and (A5), the fragmentation rate as in equation (A6) reproduces the decay of plages for solar conditions acceptably for the present purpose, as discussed in § 3.

The disappearance of magnetic flux from the surface is still shrouded in mystery: it remains unclear whether flux is retracted back into the convective envelope, is expelled from the Sun, or is milled down to small-scale, intrinsically weak fields that can be dissipated by convective mixing, or all of the above (see Zwaan 1987 for a discussion). Fortunately, this problem does not need to be understood in detail for the present purpose: both the success of the diffusion model discussed above and the successful description of the magnetic flux distribution in quiet Sun in the statistical model developed by Schrijver et al. (1997b) suggest that flux disappearance can be treated as a mathematical cancellation problem: whenever two concentrations of opposite polarity come close enough together, the smallest of the two can be assumed to disappear, while the unbalanced flux in the largest concentration survives.

A5. OTHER PARAMETERS

The simulations (listed in Table 1) are performed with time steps of 20,000 s. At a mean velocity of 0.3 km s^{-1} (§ A.4), concentrations typically move 6000 km, or somewhat more than the 4200 km radius of the "coalescence area" discussed in § A.4. This allows some concentrations to miss each other, as observed on the Sun, but most concentrations that come close together will collide. The time step is approximately 40% of the fragmentation timescale at the local minimum for $\Phi \approx 1.5 \times 10^{20}$ Mx.

The simulations are run in general for an equivalent of 360 days. The results discussed in this study are for periods covering the last 50 days (roughly two solar rotations) of the simulated period. Models for very active stars and for stars with severely truncated source spectra are run for a shorter time because of the decreased flux replacement timescale.

The time interval for the simulations is sufficient to reach statistical equilibrium in the flux histograms for the latitude domain within $\pm 60°$ (covering 87% of the stellar surface) when the flux injection peaks at a latitude near 20° (see the

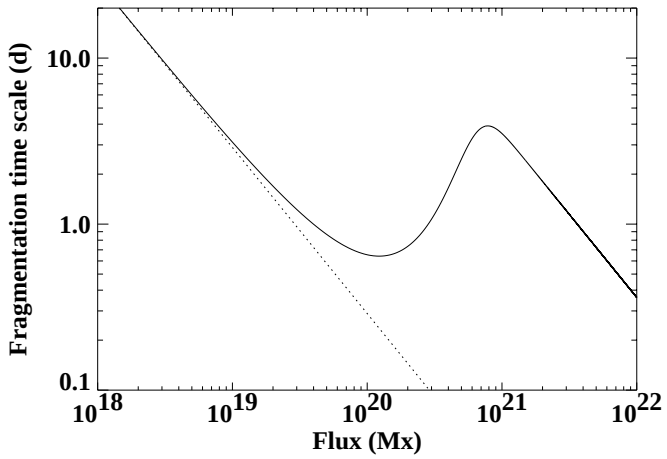

FIG. 14.—Expectation value of time to fragmentation for flux concentrations according to eq. (A6)

discussion of timescales by DeVore 1987; Sheeley 1992) on which this study focuses. That time period exceeds the global flux replacement timescale and the timescale for differential rotation. This time is long enough for the total flux and the flux histograms to converge to a quasi-stationary state. The high-latitude regions (and the patterns of the unipolar regions there) require longer simulations to be borne out properly, but they are not studied here because they contribute relatively little to the emission of active stars and because no significant observational constraints exist for the meridional flow at high latitudes for other cool stars.

The flux contained in concentrations is modeled in multiples of 1×10^{18} Mx (equivalent to a signal of 0.7 G in a KPNO-style synoptic map) to avoid the formation of a multitude of very small concentrations by incomplete cancellations. In quiet Sun, the average concentration has been measured to contain 3×10^{18} Mx (Schrijver et al. 1997b), i.e., three "units" of flux as used in the simulations.

REFERENCES

Ayres, T. R., Marstad, N. C., & Linsky, J. L. 1981, ApJ, 247, 545
DeVore, C. R. 1987, Sol. Phys., 112, 17
Donahue, R. A., Dobson, A. K., & Baliunas, S. L. 1997, Sol. Phys., 171, 191
Güdel, M. 1997, ApJ, 408, L121
Hagenaar, H. J., Schrijver, C. J., Title, A. M., & Shine, R. A. 1999, ApJ, 511, 932
Hall, D. S. 1991, in The Sun and Cool Stars: Activity, Magnetism, Dynamos, ed. I. Tuominen, D. Moss, & G. Rüdiger (Berlin: Springer), 352
Harvey, K. L. 1992, in Proc. Workshop on the Solar Electromagnetic Radiation Study for Solar Cycle 22, US Dept. of Commerce, NOAO Environmental Res. Labs., ed. R. F. Donelly (Springfield: National Technical Information Service), 113
———. 1993, Ph.D. thesis, Astronomical Instit., Utrecht Univ., chaps. 2–5
Harvey, K. L., & White, O. R. 1999, ApJ, 515, 812
Harvey, K. L., & Zwaan, C. 1993, Sol. Phys., 148, 85
Howard, R. F. 1991, Sol. Phys., 136, 251
Kitchatinov, L. L., & Rüdiger, G. 1999, A&A, 344, 911
Komm, R. W., Howard, R. F., & Harvey, J. W. 1993a, Sol. Phys., 143, 19
———. 1993b, Sol. Phys., 147, 207
Noyes, R. W., Hartmann, L., Baliunas, S. L., Duncan, D. K., & Vaughan, A. H. 1984, ApJ, 279, 763
Oranje, B. J., Zwaan, C., & Middelkoop, F. 1982, A&A, 110, 30
Peres, G., Orlando, S., Reale, F., Rosner, R., & Hudson, H. 2000, ApJ, 528, 537
Rüdiger, G., & Arlt, R. 1999, in Advances in Nonlinear Dynamos, ed. A. Ferriz-Mas & M. Jimenéz (Newark: Gordon & Breach), chap. 6
Saar, S. H. 1996, in IAU Symp. 176, Stellar Surface Structure, ed. K. G. Strassmeier & J. L. Linsky (Dordrecht: Kluwer), 237
Schrijver, C. J. 1987, A&A, 180, 241
———. 1989, Sol. Phys., 122, 193
———. 1990, A&A, 234, 315
———. 1991, in Mechanisms of Chromospheric and Coronal Heating, ed. P. Ulmschneider, E. Priest, & R. Rosner (Heidelberg: Springer), 257
Schrijver, C. J. 1992, A&A, 258, 507
———. 1993, A&A, 269, 446
———. 1995, A&A Rev., 6, 181
Schrijver, C. J., Coté, J., Zwaan, C., & Saar, S. H. 1989, ApJ, 337, 964
Schrijver, C. J., Dobson, A. K., & Radick, R. R. 1992, A&A, 258, 432
Schrijver, C. J., et al. 1996, ApJ, 468, 921
———. 1998, Nature, 394, 152
———. 1999, Sol. Phys., 187, 261
Schrijver, C. J., & Harvey, K. L. 1989, ApJ, 343, 481
———. 1994, Sol. Phys., 150, 1
Schrijver, C. J., & Martin, S. F. 1990, Sol. Phys., 129, 95
Schrijver, C. J., Mewe, R., & Walter, F. M. 1984, A&A, 138, 258
Schrijver, C. J., Title, A. M., Hagenaar, H. J., & Shine, R. A. 1997a, Sol. Phys., 175, 329
Schrijver, C. J., Title, A. M., Van Ballegooijen, A. A., Hagenaar, H. J., & Shine, R. A. 1997b, ApJ, 487, 424
Schrijver, C. J., & Zwaan, C. 2000, in Solar and Stellar Magnetic Activity (Cambridge: Cambridge Univ. Press), chaps. 8, 9, and 12.7
Sheeley, N. R. 1992, in ASP Conf. Ser. 27, The Solar Cycle, ed. K. L. Harvey (San Francisco: ASP), 1
Sheeley, N. R., Boris, J. P., Young, T. R., DeVore, C. R., & Harvey, K. L. 1983, in IAU Symp. 102, Solar and Stellar Magnetic Fields: Origins and Coronal Effects, ed. J. O. Stenflo (Dordrecht: Reidel), 273
Sheeley, N. R., Nash, A. G., & Wang, Y.-M. 1987, ApJ, 319, 481
Simon, G. W., Title, A. M., & Weiss, N. O. 1995, ApJ, 442, 886
Wang, Y.-M., Nash, A. G., & Sheeley, N. R. 1989, Science, 245, 712
Worden, J., & Harvey, J. W. 2000, Sol. Phys., 195, 247
Zwaan, C. 1981, in Solar Phenomena in Stars and Stellar Systems, ed. R. M. Bonnet & A. K. Dupree (Dordrecht: Reidel), 463
———. 1987, ARA&A, 25, 83
Zwaan, C., & Harvey, K. L. 1994, in Solar Magnetic Fields, ed. M. Schüssler & W. Schmidt (Cambridge: Cambridge Univ. Press), 27